Eur. Phys. J. B (2018) 91: 138
https://doi.org/10.1140/epjb/e2018-90060-6

THE EUROPEAN PHYSICAL JOURNAL B

Regular Article

Pentameric PdAu and PdPt nanoparticles on the MgO(1 0 0) surface and their CO and O_2 adsorption properties[⋆,⋆⋆]

Mikail Aslan[1] and Roy L. Johnston[2,a]

[1] Department of Metallurgical and Materials Engineering, Gaziantep University, Gaziantep, Turkey
[2] School of Chemistry, University of Birmingham, Edgbaston, Birmingham B15 2TT, UK

Received 7 February 2018 / Received in final form 27 April 2018
Published online 2 July 2018

Abstract. The surface mode of the Birmingham Cluster Genetic Algorithm (S-BCGA), which performs an unbiased global optimisation search for clusters adsorbed on a surface, has been employed for the global optimisation of noble metal pentamers on an MgO(1 0 0) substrate. The effect of element identity and alloying in surface-bound neutral subnanometre particles is calculated by energetic analysis of all compositions of supported 5-atom PdAu and PdPt clusters. Our results show that the binding strengths of the component elements to the surface are in the order Pt > Pd > Au. In addition, alloying Pd with Au and Pt is favorable for this size since excess energy calculations show a preference for bimetallic clusters for both cases. Furthermore, the electronic behaviour, which is intermediate between molecular systems and bulk metals allows tuning of the characteristics of particles in the subnanometre size range. The adsorption of CO and O_2 probe molecules are also modelled and it is found that CO and O_2 adsorption leads to a weakening of the cluster–surface interaction.

1 Introduction

The adsorption of transition metal clusters and nanoparticles supported on oxide surfaces includes materials with varied technological applications in microelectronic components [1], metal-ceramic composites [2], gas sensors [3], corrosion protection [4], and heterogeneous catalysis [5]. In these applications, understanding of supported small (subnanometre) metal clusters is aided by study of cluster nucleation and growth, mobility and catalytic activity. For metal cluster catalysts, modification of particle size, geometry and electronic structure, as well as the nature of the support, allows tuning of the properties of the catalytic site(s), in order to achieve the desired activity and/or selectivity for specific transformations [6]. Surprisingly, researchers have found examples of increased lifetimes (more catalytic cycles) and selectivity of reactions catalyzed by subnanometer clusters compared to larger (subnanometre and above) sizes, in particular for Pt [7,8], Pd [9,10], Ag [11] and Au [12]. In order to comprehend the chemical and physical properties that give rise to these effects, as well as to establish relationships between the structure and size of the catalyst particles and their reactivity, this information is of particular importance for very small particles, whose properties cannot be predicted by scaling laws [13]. In this regard, heterogeneous catalysis by subnanometer metal clusters is presently attracting a great deal of attention from both the theoretical [14] and experimental communities.

Modification of the catalytic action of a metal cluster by the oxide support may have significant effects on catalyst design and opens the possibility of developing more active and/or selective catalysts. The adsorption of a subnanometer sized metal particles upon an oxide surface may leads to major modifications of the electronic structures of these species. In particular, charges may shift from the surface to the supported metal or vice versa. This is the basis for the electronic metal–support interaction which may modify the chemical activity of very small catalytic nanoparticles. For instance, the catalytic activity of palladium clusters on MgO and Al_2O_3 surfaces was found to be controlled at the single Pd–Pd bond level, in which the role of the surface and the geometry of the cluster are both factors [15]. Lee et al. [16], in their combined theoretical and experimental study, showed the effect of palladium cluster size on methanol decomposition upon an amorphous alumina support. Grönbeck and Broqvist [17] characterized the interaction of Pt atoms on BaO and MgO surfaces with respect to preferred geometrical configurations and electronic structures, showing that Pt atoms bind more strongly to BaO surfaces than MgO surfaces.

To see the effects of the oxide support, we have chosen a MgO(1 0 0) support in this study. MgO is an ideal support for studying metal cluster–substrate interactions, since it is relatively easy to prepare with a high quality

⋆ Contribution to the Topical Issue "Shaping Nanocatalysts", edited by Francesca Baletto, Roy L. Johnston, Jochen Blumberger and Alex Shluger.

⋆⋆ Supplementary material in the form of one pdf format file available from the Journal web page at https://doi.org/10.1140/epjb/e2013-40008-5.

[a] e-mail: r.l.johnston@bham.ac.uk

(1 0 0) surface that acts as perfect background for electron microscopy measurements [18,19]. It is also non-polar and it is a stable, geometrically simple substrate without the complications associated with surface reconstruction. Sterrer et al. [13] reported that by manipulation of adatoms with a scanning tunnelling microscope tip small Pd particles adsorbed on MgO can be created and subsequently characterized with experimental control over the stoichiometry and the adsorption sites of the particles. Sanchez et al. [20] performed temperature-programmed reaction studies of the catalyzed combustion of CO on size-selected small Au_n ($2 \leq n \leq 20$) gold clusters deposited on MgO(1 0 0). Subnanometer gold particles on MgO have excellent catalytic activity and Au_8 was found to be the smallest catalytically active cluster. Li et al. [21] revealed that gold nanoparticles decorated on MgO nanosheets have increased catalytic activity for solvent-free benzyl alcohol aerobic oxidation. In their TEM images, the gold nanoclusters have a hemispherical geometry. The high activity of Au/MgO is due to the properties of the support and/or those of the gold–support interface. The mapping of the potential energy surface indicated that monomer diffusion at room temperature is unlikely on both supports. Sementa et al. [22] found that the intermediate carbonate species $Ag_3(CO_3)$ formed on the MgO(1 0 0) surface during the oxidation of CO on supported silver trimers and is probably the actual catalyst. They also investigated whether such a species may be the catalyst for various other reactions. Barcaro and Fortunelli [23] showed that alloying Cu, Au and Pd with Ag on a double vacancy MgO substrate allowed the selective recovery of electronic and geometric magic numbers, and control of the stability of the particle upon the surface. Davis et al. [24] characterized AuIr sub-nanoalloys in the presence of the MgO(1 0 0) surface by using the parallel pool methodology. In their study, the MgO(1 0 0) surface was also found to influence the atomic ordering and spin of the AuIr clusters.

To enable the systematic study of CO oxidation to CO_2 on supported clusters, the O_2 and CO adsorption properties on different sizes of clusters must first be explored [25]. The CO molecule is often used as a probe molecule to classify the electronic natures and binding capabilities of metal surface sites [26]. The use of CO therefore allows characterization of the local structure of subnanometre and nanoalloy catalysts, which is critical in understanding their chemical properties. Li et al. [27] studied CO oxidation promoted by gold-titanium bimetallic oxide cluster anions They found that Au–TiO_2 cluster anions are more active than pure titanium oxide cluster anions for CO oxidation. Negreiros et al. [28] studied the catalytic properties of Ag_mAu_n ($m+n \leq 3$) clusters on the MgO(1 0 0) substrate and found that, in terms of efficiency and stability, the Ag_2Au_1 mixed cluster is a good catalyst for CO oxidation. In addition, Wang et al. [29] studied the catalytic properties of CO oxidation on free PtAu clusters, with up to 4 atoms, using DFT calculations, and demonstrated that for CO oxidation, free Pt–Au clusters are more active than pure Pt or Au clusters. Duan and Henkelman [30] showed that the interaction of the Au on the MgO surface has an important effect on the activation of O_2 molecules since it promote charge transfer to the antibonding O_2 $1\pi_g^*$ molecular orbital. Halim et al. [31] studied the binding and activation of CO molecules on Pd atoms supported on MgO, CaO, SrO and BaO substrates. They found that CO adsorption on Pd is enhanced considerably in the presence of the MgO support.

The rarity of studies related to the Pd_nX_{5-n} (X = Au, Pt)/MgO(1 0 0) systems, including CO and O_2 adsorption, has led us to select them for our study. Control of reactivity for such systems has been explored as a function of cluster size and surface defects [32–34], but less well studied are the mixed metal particles, in which both composition and chemical order provide additional tunable parameters for the design of particles with specific properties [35], due to the difficulty of the experimental production of mixed metal systems. Furthermore, bimetallic catalysts may show better catalytic stabilities and selectivities, compared with monometallic clusters. According to experiments, alloying a second metal with Pd can lead to higher catalytic activity due to the ligand effect [36] (electronic modifications, associated with the additional metal) and the ensemble effect [37,38] (the additional metal may block certain sites, reducing or eliminating the formation of an inhibiting species or an intermediate in a competing reaction [39]). Theoretical studies of ultra-small mixed noble metal clusters upon MgO [23,28,40] have found that control of composition may have a drastic effect on structure, and thus reactivity. Another motivation is that examination of the bonding in smaller (subnanometre) bimetallic clusters can only be achieved using electronic structure methods. Subnanometre clusters upon an oxide substrate, allow a synergistic combination of quantum size effects (which require electronic structure methods to reproduce) and sufficiently small particle sizes to allow for direct GO at the DFT level [41]. Thus, electronic structure calculations are necessary to estimate the correct growth characteristics of NPs.

In this work, we use the electronically stable MgO surface which allows a detailed study of both the subnanometre cluster geometries on the surface and the adsorption of CO and O_2 molecules. These will be discussed in detail below, with the aim of understanding how the catalytic activity and selectivity of subnanometre clusters can be modified by the substrate. Here, we use the Surface Birmingham Cluster Genetic Algorithm (S-BCGA) to predict the global minimum (GM) structure of the studied particles for bimetallic pentamer clusters over the entire composition range, using the Genetic Algorithm-Density Functional Theory (GA-DFT) approach. DFT-based global optimization (GO) is a computational tool which produces accurate results that can provide data that is not available experimentally and can support available experimental data at a fundamental level. Such data may include charge transfer, binding energies, adsorption energies and mobility.

2 Methodology

Possible geometric isomers can be generated by intuition but this is challenging for larger systems and also leads to biased results. A better technique to find GM is to use an algorithm that generates unbiased geometric isomers. For this reason, there is available some computational methods, such as statistical mechanical methods [42], basin hopping [43] and genetic algorithms (GA) [44]. Which computational methods should be used depends on how the potential energy surface is described and how complex it is [42]. After the optimisation of the NP structure using these methods, for free or supported NPs, reoptimisation at the Density Functional Theory (DFT) level can be performed so as to correlate the predicted lowest energy structure with experimental results. A detailed description of this approach has been presented in our previous [41,45].

In this study, the GM structures are determined by combining two methodologies: the S-BCGA [41] and Density Functional Theory, using an interface to the PWscf code of Quantum Espresso (QE) software [46]. S-BCGA provides an unbiased search starting from entirely random coordinates for the structures of Pd_nX_{5-n} (X = Au, Pt) nanoalloys for all compositions, which predicts the most stable cluster that can be grown on the substrate or the result of allowing a gas phase deposited cluster to anneal on the surface. The interface with QE enables the energy landscape of a system to be searched for the GM at the DFT level. The DFT calculations include scalar relativistic effects and ultrasoft RRKJ-type pseudopotentials [47] for carbon, oxygen and all metallic elements except for magnesium atoms. A norm-conserving Vanderbilt pseudopotential [48] is used for magnesium atoms. We have adopted the Perdew–Burke–Ernzerhof (PBE) GGA exchange–correlation functional [49] that has been widely used in the treatment of small, mixed clusters. For the primary screening of the structures with S-BCGA, the default density cutoff convergence criterion is applied with energy cutoff of 20 Ry for an adequate convergence. An electronic convergence criterion of 10^{-5} Ry, with the Methfessel–Paxton smearing scheme [50] having a value of 0.01 Ry to improve the SCF convergence of metallic system, was implemented. Gamma point calculation have been used for a wide range of studies of MgO-supported clusters and we have found gamma-point DFT calculations to be sufficient for this study (see Supplementary Information).

For local geometry optimization, the BFGS algorithm in QE is applied, with convergence corresponding to when the differences between energies and total forces for successive structures drop below 10^{-4} Ry and 10^{-3} Ry a_0^{-1}, respectively. In the S-BCGA program, the crossover process (to generate a predetermined number of offspring) uses the roulette wheel selection criterion and the Deaven–Ho cut and splice method [44]. The calculations have been performed within a cuboidal supercell of 11.7 Å × 11.7 Å × 29.25 Å, leaving 14.7 Å of vacuum between slabs in the z-direction, which provides sufficient space to avoid spurious image–image interactions. The cluster structures are generated at least 2 Å above a rigid surface of an ideal MgO(1 0 0) surface comprising two MgO layers that have been found to be adequate for the recovery of accurate bond lengths, energies and electronics in several investigations at the GGA-DFT level [17,41,51]. The MgO lattice is fixed during the cluster optimizations. The reason for keeping the MgO lattice fixed is the slab is modelling the surface of bulk MgO. Also, small sized-noble metal clusters have a negligible effect on the geometry of MgO(1 0 0) surface, as supported by our previous study [15]. To test this in our calculation, we have optimized Au_5 clusters on the relaxed MgO(1 0 0) surface, giving a total energy of −21657.257 eV, while the energy of Au_5 on the unrelaxed MgO surface is −21652.723 eV. These small differences (0.02%) can be neglected, and we find there are no important geometrical changes between these structures.

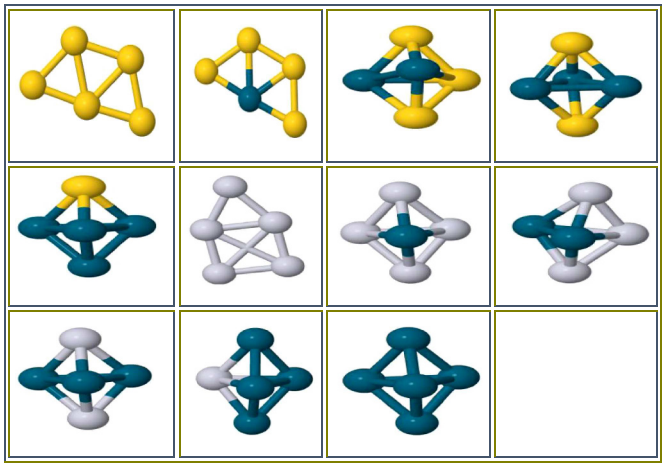

Fig. 1. Structures of the lowest energy configuration for each composition of Pd_nAu_{5-n} and Pd_nAu_{5-n}. Au, Pd, and Pt are colored gold, cyan and white, respectively.

After the GA has converged (when the lowest energy member of the population does not change for 200 generations), using an interface to the PWscf code of the Quantum Espresso (QE) software [46], spin-polarised reminimizations of S-BCGA-DFT global minima were carried out with tighter convergence criteria. The self consistency convergence cutoff is reduced to 10^{-8} Ry. The plane wave basis is expanded to 50.0 Ry for all atoms, with a charge density cutoff of 500.0 Ry. The smearing parameter is reduced to 0.005 Ry, so as to reproduce metallic states more accurately. Electron total magnetizations ranging from 0 to 3 μ_B are considered for all reminimization calculations since, Pd, Pt and Au clusters do not typically show large magnetic moments, in contrast to elements such as Rh and Ir.

By applying the same convergence criteria, the adsorption of CO and O_2 is modelled by the attachment of the adsorbate to each available binding site upon the GM cluster for each composition and then performing a local geometry optimization.

3 Results and discussion

The putative GM structures for each composition of gas phase and supported Pd_nAu_{5-n} and Pd_nPt_{5-n} clusters are shown in Figures 1 and 2, respectively, and other

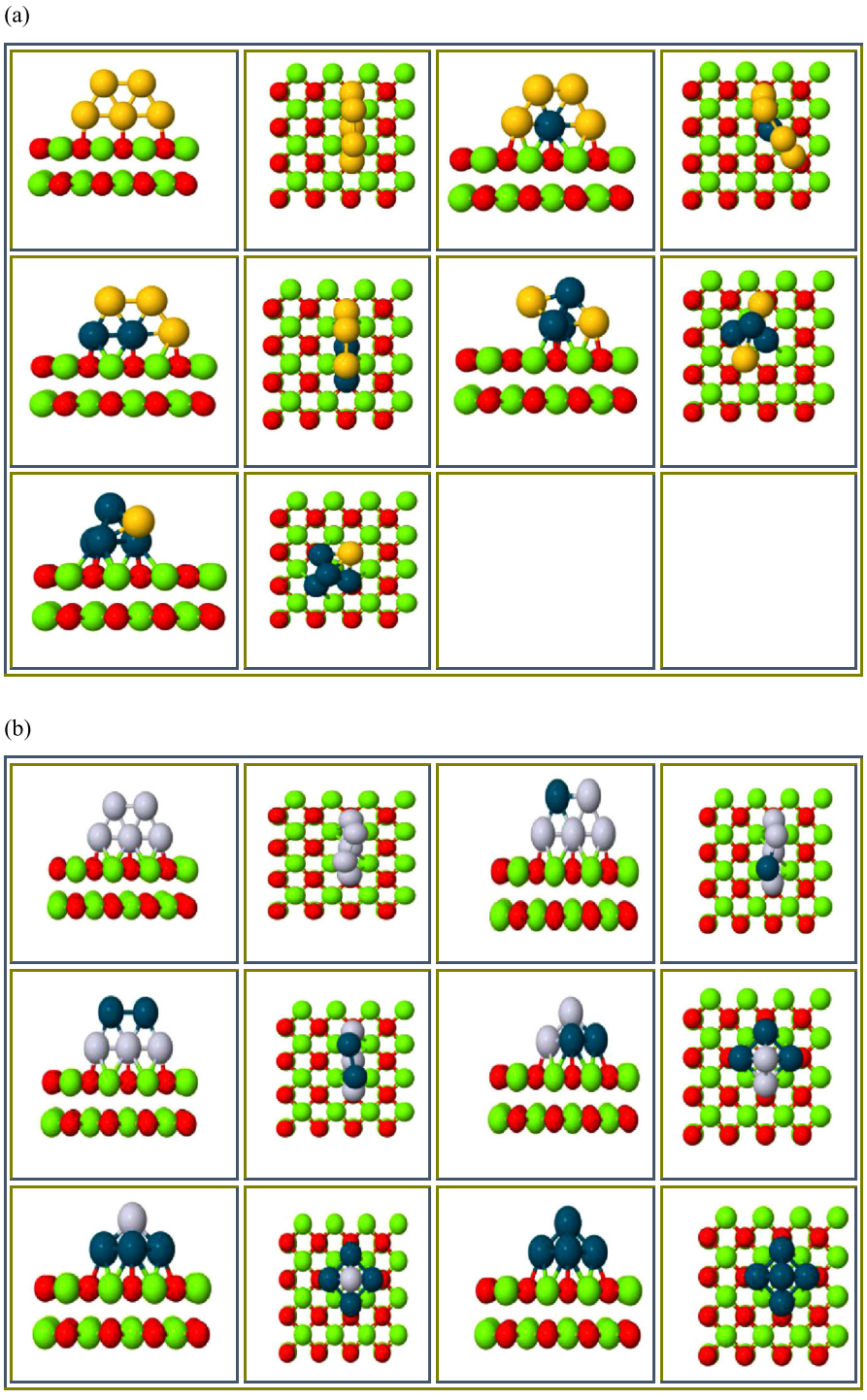

Fig. 2. Structures of the lowest energy configuration for each composition of (a) Pd_nAu_{5-n} and (b) Pd_nPt_{5-n} on MgO(1 0 0). Au, Pd, Pt, Mg and O are colored gold, cyan, white, green and red, respectively.

properties of the supported PdAu and PdPt clusters are reported in Table 1.

To investigate the strength of metal–substrate bonding, we optimized single Au, Pd and Pt atoms and pure metal pentamers (Au_5, Pd_5 and Pt_5) on the MgO(1 0 0) surface at the DFT level. All single metal atoms favor atop oxygen binding site on the MgO substrate and the calculated interaction energies are: 0.95 eV (Au); 1.42 eV (Pd) and 2.42 eV (Pt), which are in excellent agreement with previous calculations [52–54]. The pentameric clusters also coordinate to the substrate via M–O interactions (see Fig. 2). The metal–MgO oxygen bond distances for supported metal atoms (M_1) and pure pentameric clusters (M_5) are compared in Table 2, along with the difference

Table 1. Properties of supported pentameric PdAu and PdPt nanoparticles.

Supported species	(2S+1)	E_{xs}/eV	E_{ie}/eV	E_{ads}(CO)/eV	E_{ads}(O_2)/eV
Au_5	2	0.00	1.69	0.95	1.58
Pd_1Au_4	1	2.75	2.27	1.10	0.80
Pd_2Au_3	2	3.36	2.77	1.59	1.75
Pd_3Au_2	3	1.39	2.08	1.58	2.00
Pd_4Au_1	2	1.28	2.32	2.66	2.36
Pd_5	1	0.00	2.54		1.65
Pt_5	1	0.00	4.10	2.37	2.32
Pd_1Pt_4	1	0.96	4.17	2.13	2.18
Pd_2Pt_3	1	1.68	3.91	2.24	3.49
Pd_3Pt_2	1	0.10	3.12	1.78	2.14
Pd_4Pt_1	1	1.17	3.00	1.37	1.77

E_{xs}: excess (mixing) energy, E_{ie}: interaction energy, E_{ads}: adsorption energy.

Table 2. Metal–MgO oxygen distances (Å) for supported M_1 atoms and M_5 nanoparticles and the differences between them.

Supported species	r_1 (M_1–O)	r_5 (M_5–O)	r_5–r_1
$Au_{1,5}$	2.57	2.42	−0.15
$Pd_{1,5}$	2.31	2.46	0.15
$Pt_{1,5}$	2.32	2.18	−0.14

in the M–O distance between the monomer and the pentamer.

Going from M_1 to M_5, Au–O and Pt–O bonds get shorter, while Pd–O bonds get longer. It can therefore be inferred that for ultra-small sizes, in the case of increasing cluster size, the mobility of Pd clusters on MgO(1 0 0) may be increased. This is supported by previous studies [52,55].

3.1 Supported PdAu and PdPt nanoparticles

From Au_5 to Pd_2Au_3, the MgO-supported GM structures for pentameric PdAu clusters have planar geometries and lie approximately perpendicular to the plane of the surface. This orientation is due to the "metal-on-top effect" which is commonly observed for sub-nanometre clusters of platinum group and noble metal clusters on MgO [56]. The planar structures, which are also found for the gas phase Au_5 and Pd_1Au_4 clusters (Fig. 1) are stabilised due to relativistic effects which lead to stronger *s*–*d* hybridization and *d*–*d* interactions in Au than Pd [57]. According to the study of Ismail et al. [58] for Pd-rich PdAu nanoparticles, excellent epitaxial growth of Pd is observed on MgO(1 0 0), so this may also play a role in stabilising certain configurations. For bimetallic Pd–Au pentamers, the MgO(1 0 0) surface has little effect on the geometric structure, compared to the gas phase global minimum, with the exception of Pd_2Au_3.

Our calculations predict that the Au_5 cluster has a planar trapezoid structure, both in the gas phase and on the MgO support. In agreement with our calculations, the gas phase structure of Au_5 has previously been shown to have the same structure [59,60]. This cluster interacts with the MgO surface quite weakly (with a calculated interaction energy of 1.69 eV) compared to the other clusters studied. The high ionization potential of gold disfavors charge transfer from Au to the surface, which leads to weakened Au-surface bonding and minimal effect of the substrate on the cluster geometry.

On doping Pd atoms into Au_5, the bonding strength of Pd to surface oxygen is stronger than that of Au so Pd atoms preferentially bind to the substrate (i.e. lying at the cluster–substrate interface). In the case of Pd_1Au_4, the Pd atom occupies the higher coordinated central position in the line of three atoms bound to MgO, while Au atoms prefer the lower coordinated outer sites. This is due to the fact that Pd–Au bonds are stronger than Au–Au bonds. Supported Pd_2Au_3 also has a trapezoid structure, with 2 Pd atoms at the cluster–MgO interface and a Pd–Pd bond (which is stronger than Pd–Au and Au–Au bonds), though the gas phase structure of Pd_2Au_3 has trigonal bipyramidal structure (Fig. 1). Presumably the 2D trapezoid structure is a low-lying metastable isomer for Pd_2Au_3, so the greater cluster–surface interaction possible (due to the metal-on-top effect and the stronger Pd–O bonding) drives the cluster restructuring. Replacing another Au atom by Pd, results in a change of the surface-bound cluster topology from 2D to 3D, yielding a trigonal bipyramidal (TBP) structure for Pd_3Au_2. The Au atoms occupy the low connectivity axial sites in this structure, with the Pd atoms occupying the higher connectivity equatorial sites. In this case, this arrangement (which is driven by the stronger Pd–Au bonds) is also found for the supported cluster, winning out energetically over an alternative TBP isomer where the three Pd atoms occupy 2 equatorial and 1 axial site (forming a triangular face of the polyhedron), which would enable all three Pd atoms to bind to the MgO substrate, or a trapezoid structure with three co-linear Pd atoms bound to the substrate. The binding of Pd_3Au_2 to the MgO surface is via two Pd and one Au atom. Pd_4Au_1 has a distorted square pyramidal geometry in the gas phase, with the Au atom in the lower coordinate distorted square face. This arrangement is also favoured on the MgO surface, where a Pd_3 triangular face of the pyramid binds to the MgO(1 0 0) surface. The pure Pd_5 cluster adopts a slightly distorted TBP structure in the gas phase but it becomes a square pyramidal structure on the surface, where the square face sits approximately over four O atoms.

Weak interactions between the adsorbate and substrate generally leads to 3D structural configurations (where there are more metal–metal bonds), corresponding to Volmer–Weber (VW) film growth [61]. In a similar way, a study conducted by Hu et al. [62] indicated that VW type deposition is observed for pure Ag_5 deposited on MgO. The relatively weak interaction between the pure pentameric Pd cluster and the MgO substrate (1.97 eV) indicates that the effect of the MgO substrate is not the most important factor affecting Pd cluster growth. Similar results have been found for smaller pure Pd clusters (Pd_3 and Pd_4) on MgO(1 0 0) by Giardiona and Pacchioni [54]. This is relevant to the early stages of nucleation and growth of pure Pd clusters on the MgO substrate.

The MgO(1 0 0) surface has a strong effect on the geometries of pentameric PdPt clusters (Fig. 3), compared to the lowest energy gas phase structures. Gas phase Pt_5 was predicted to have a 3D square pyramidal structure by Wang and Gao [63]. This is in disagreement with our study (and some other studies [64,65]), in which the structure is found to be a 2D edge-bridged square. The gas phase structures of Pt_5, Pd_1Pt_4 and Pd_2Pt_3 all become pseudo-planar trapezoid structures on the MgO substrate, lying perpendicular to the surface. Due to relativistic effects for the heavy Pt atom, in the gas phase there is a small energy separation between the most stable 3D and the alternative 2D structures for Pt-rich clusters. This is overcome by the stronger interaction with the MgO substrate, which favours the planar structures (due to the metal-on-top effect). In contrast, the supported Pd-rich clusters have 3D structures, both in the gas phase and when supported on MgO.

As mentioned above, the supported pure Pt_5 cluster has a similar trapezoidal structure to Au_5 (though with the top two atoms twisted slightly relative to the three atoms bonded to the substrate). In the experimental study of Watanabe et al. [66], for Pt_n clusters on the TiO_2(1 1 0) surface, scanning tunneling microscopy measurements indicate that for $n < 7$, the clusters have 2D structures and lie flat on the surface (TiO_2 is a more reactive surface than MgO and the perpendicular geometries are not stabilised), while larger clusters adopt 3D structures.

In contrast to the PdAu clusters, in the PdPt case the Pt atoms tend to occupy more central, higher coordinated sites, while Pd atoms generally prefer lower coordinated outer sites. However, it is also important to consider the number of homo- and heteronuclear bonds, as the slightly distorted TBP gas phase structures of Pd_1Pt_4 and Pd_2Pt_3 (Fig. 1) both have Pd atoms in the higher connected equatorial sites, and do not have the maximum number of strong Pt–Pt bonds: instead they maximise the number of intermediate strength Pt–Pd bonds. For supported Pd_1Pt_4 and Pd_2Pt_3, the slightly twisted trapezoidal structure is again found, with three Pt atoms bound to the substrate and the Pd atoms occupying lower coordinated sites in the second layer. These configurations can be explained by the order of metal–metal bond strengths: Pt–Pt > Pt–Pd > Pd–Pd and the greater strength of Pt–O compared to Pd–O bonding. In this regard, the presence of Pt atoms in clusters strengthens the interaction with the MgO surface and reduces the diffusion of the clusters on the substrate, thereby increasing the stability of the clusters with respect to sintering.

On replacing another Pt atom by Pd, there is a conversion to a 3D distorted square pyramidal structure for supported Pd_3Pt_2, with one Pt occupying the higher connectivity apical site (maximising metal–metal binding) and the other being in the basal plane (which binds to the substrate). The gas phase structure has a similar geometry, but with both Pt atoms in the basal plane, a structure which sacrifices the strongest Pt–Pt bond but has fewer weak Pd–Pd bonds and again maximises the number (6) of intermediate strength Pt–Pd bonds. In the gas phase, Pd_4Pt_1 has a TBP structure, with the Pt atom in a higher coordinated equatorial site. The supported Pd_4Pt_1 cluster, however, has a square pyramidal structure, with Pt occupying the higher connectivity apical site, though this is not in contact with the MgO substrate. This again maximises metal–metal binding and the loss of the Pt–O binding interaction is outweighed by the better pseudo-epitaxy between the Pd_4 basal plane and the MgO lattice, as mentioned above.

3.2 Analysis of surface binding of supported PdAu and PdPt nanoparticles

To further examine the stability of supported clusters and the strength of their binding to the MgO(1 0 0) substrate, we have calculated excess energies and interaction energies for the supported pentameric clusters, for all compositions.

The effect of mixing (or alloying) in a supported bimetallic cluster can be studied by calculating the excess energy, E_{xs}, that gives a measure of the stability of the supported bimetallic clusters with respect to supported monometallic clusters:

$$\begin{aligned} E_{xs} = &-N\,E(\mathrm{MgO} + \mathrm{Pd}_m\,\mathrm{Au}_m/\mathrm{Pd}_m\,\mathrm{Pt}_n) \\ &+m\,E(\mathrm{MgO} + \mathrm{Pd}_N) + n\,E(\mathrm{MgO}) \\ &+\mathrm{Au}_N/\mathrm{Pt}_N, \end{aligned} \tag{1}$$

where $E(\mathrm{MgO} + \mathrm{Pd}_m\,\mathrm{Au}_n/\mathrm{Pd}_m\,\mathrm{Pt}_n)$ is the ground state energy of the supported clusters and $E(\mathrm{MgO} + \mathrm{M}_N)$ is the lowest energy of the pure supported clusters (M = Pd, Au, Pt), with $N = m + n = 5$. For gas phase (free) clusters, E_{xs} is equivalent to a mixing energy, with favourable mixing corresponding to positive values of E_{xs} and negative values indicating a demixing tendency. For supported clusters, in addition to the excess energy, E_{xs} also reflects differences in the strength of binding of the clusters to the substrate.

Figure 3a shows excess energy plots as a function of composition. All bimetallic clusters are more stable than the monometallic ones ($E_{xs} > 0$), which means there is a thermodynamic driving force towards the formation of supported bimetallic clusters. For gold-rich compositions, the supported bimetallic PdAu clusters exhibit high excess energies of 2.75 eV for Pd_1Au_4 and 3.36 eV for Pd_2Au_3. The large drop in E_{xs} on going to Pd_3Au_2 and Pd_4Au_1 reflects the change from 2D to 3D structures and the

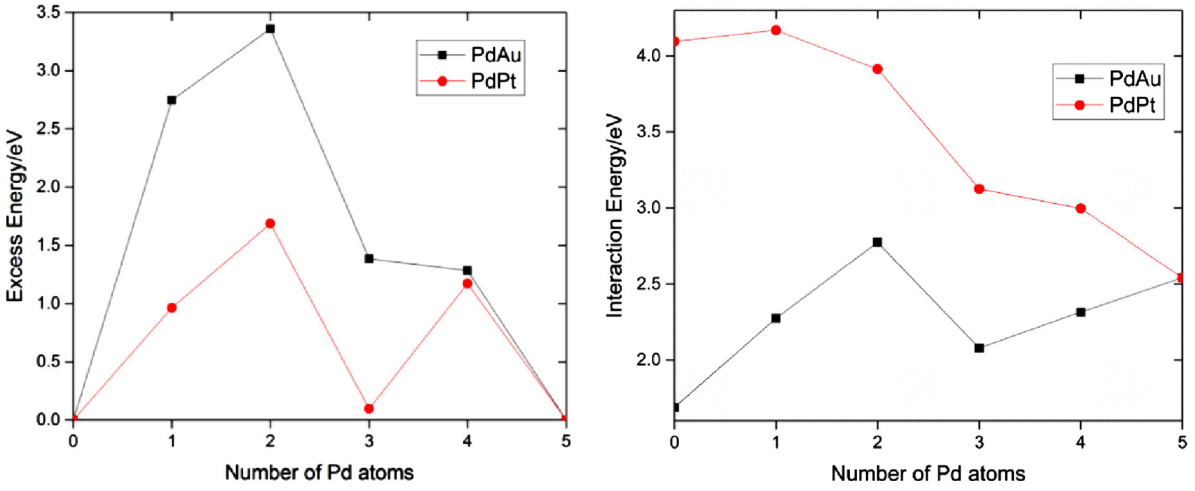

Fig. 3. (a) Excess energies (E_{xs}) and (b) interaction energies (E_{ie}) for each composition of pentameric PdAu and PdPt clusters supported on MgO(1 0 0).

conflict between maximising M–M and M–O binding, as discussed above.

Excess energy values for the PdPt clusters (which peak at around 1.7 eV for Pd_2Pt_3) are significantly smaller than for AuPd, perhaps due to the significantly stronger Pt–Pt bonding (stabilising the pure Pt_5 cluster). This excess (mixing) energy tendency can also be explained in terms of the larger bulk cohesive energy of Pt (5.84 eV/atom) compared to Pd (3.89 eV/atom) and Au (3.81 eV/atom) [67]. The large drop from Pd_2Pt_3 to Pd_3Pt_2 again coincides with the change from a 2D to 3D structure, though the significant rise to Pd_4Pt_1 ($E_{xs} = 1.17$ eV) may reflect the stronger cluster–substrate binding due to the near epitaxy between the Pd_4 basal plane of the square pyramid and the MgO(1 0 0) surface. According to the study performed by Davis et al. [68], there is strong demixing character in the Pd–Ir system (which would be expected to be similar to the Pd–Pt case) for supported clusters, due to the much stronger binding of Ir to the oxide support [67] (in fact this is significantly greater than Pt–O binding).

The energetics of the binding of clusters to the substrate is quantified by the interaction energy, E_{ie}, which is the difference between the energy of supported cluster, and the sum of energies of the surface of MgO and the gas phase cluster fixed at that geometry:

$$E_{ie} = -E(\mathrm{MgO} + \mathrm{cluster}) + E(\mathrm{MgO}) + E(\mathrm{cluster}). \quad (2)$$

In the case of monomer adsorption, moving across and down in the periodic table, Pašti et al. [69] found that the overall trend is an increase of interaction energies, E_{ie}. Pauli repulsion between filled electronic shells, orbital overlap between metal $s(d)$-states and O $2p$-states, and adsorbate polarization at the substrate are three main factors affecting interaction energies, E_{ie}. According to our calculations, as mentioned above, the interaction energies for single metal atoms on MgO(1 0 0) are in the order Pt > Pd > Au, which is in agreement with the findings of Pašti et al. [69] and Neyman et al. [70]. For the interaction of pure metal pentamer clusters on MgO, the energy ordering does not change. Normally, it is expected that $5d$-metal clusters (such as Au) on the MgO surface should have the highest E_{ie} values, whereas the $4d$-metal clusters (such as Pd) form the weakest bonds, though there are some exceptions, such as the stronger binding of Pd than Au to MgO. An explanation for this is that the surface-induced polarization of Pd is higher than that of Au [70].

Supported Pt-rich clusters exhibit significantly stronger binding than Au-rich clusters on MgO: E_{ie} (Pt_5) = 4.1 eV; E_{ie} (Au_5) = 1.6 eV. In fact, all PdPt clusters have higher interaction energies than their PdAu counterparts, including Pd_4Pt, which has four Pd atoms bound to MgO, rather then three for supported Pd_4Au. Consistent with the excess energy plots, there is a significant drop in E_{ie} accompanying the 2D–3D transition on going from Pd_2X_3 to Pd_3X_2 (X = Au, Pt). Although, the pure pentameric Pd cluster is bound more strongly to the surface (E_{ie} (Pd_5) = 2.54 eV) than Au_5, Pd_2Au_3 has a higher interaction energy (2.77 eV) than Pd_5, which may be due to an additional polarization contribution to the interaction energy. This may also explain why E_{ie} for Pd_1Pt_4 is slightly higher than that of Pt_5, though it should be noted that the interaction energies for Pt_5 to Pd_2Pt_3 are very similar, because all three clusters have the same (perpendicular) trapezoid structure with three Pt atoms bound to the MgO surface.

3.3 Magnetism of supported nanoparticles

We have investigated a range of spin states by reminimizing the GM of the supported pentameric clusters (see Supplementary Information), for different total spins (S). The optimum spin multiplicities (2S+1) of the various isomers of supported Pd_nX_{5-n} (M = Au and Pt) clusters are listed in Table 1. Small metal clusters may exhibit high magnetic moments, even for metals that are non-magnetic in the bulk [71]. In this study, for each composition, the lowest possible spin is most favourable except for Pd_3Au_2, which is predicted to be have a triplet, rather than a

Table 3. Bond length variations (Å) of M–O*(MgO), M–C(CO), and C–O(CO) bonds, comparing adsorption of CO on supported M_1 and M_5.

Species	Δr_1	Δr_5	$\Delta r_{1\to5}^{MO}$	$\Delta r_{1\to5}^{MC}$	$\Delta r_{1\to5}^{CO}$
$Au_{1,5}$	0.232	0.211	0.064	0.082	0.014
$Pd_{1,5}$	0.234	0.226	0.375	0.155	0.049
$Pt_{1,5}$	0.146	0.174	0.028	0.195	0.769

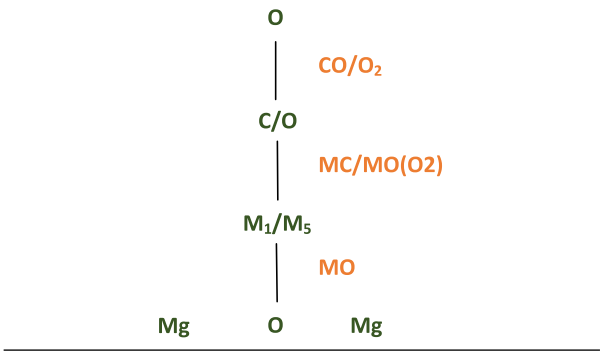

singlet ground state. The lowest energy structures of all the supported PdPt clusters have zero spin (2S+1 = 1) since the presence of Pt atoms and coordination to the substrate are found to lead to quenching of the magnetism.

3.4 CO and O_2 adsorption on supported PdAu and PdPt nanoparticles

We define the CO (or O_2) adsorption energy on a MgO-supported cluster (or supported single metal atom) as the difference between the total energy of the supported cluster with adsorbed CO (O_2) and the sum of the total energies of the supported cluster and the free CO (O_2) molecule:

$$E_{ads}(\mathrm{Mol}) = -E(\mathrm{MgO + cluster + Mol}) + E(\mathrm{MgO + cluster}) + E(\mathrm{Mol}), \quad (3)$$

where Mol = CO or O_2. A positive value of E_{ads} corresponds to exothermic adsorption.

To study the adsorption of CO and O_2 molecules on supported Pd_5, Pt_5 and Au_5 clusters, we first calculated CO and O_2 adsorption energies on single Pd, Pt and Au atoms supported on the MgO(1 0 0) surface. The M-CO adsorption energies are: 2.46 eV (Pd); 3.46 eV (Pt) and 0.80 eV (Au) and the M-O_2 adsorption energies are 1.73 eV (Pd); 2.52 eV (Pt); and 1.85 eV (Au).

E_{ads} values for CO and O_2 adsorption on the pure pentameric clusters are listed in Table 1 and plotted in Figure 1. For adsorption on the GM supported clusters, the binding of a CO or O_2 molecule is tested on each cluster atomic and bridging site. The initial adsorption sites for both CO and O_2 are taken as pointing radially outward from the cluster and then the MgO–cluster–Mol system is relaxed (energy minimized). The resulting lowest energy binding configurations are shown in Figure 5.

Table 4. Bond length variations (Å) of M–O*(MgO), M–O(O_2) and O–O(O_2) bonds, comparing O_2 adsorption on supported M_1 and M_5.

Species	Δr_1	Δr_5	$\Delta r_{1\to5}^{MO}$	$\Delta r_{1\to5}^{MO(O_2)}$	$\Delta r_{1\to5}^{O_2}$
$Au_{1,5}$	0.093	0.235	0.142	0.193	0.011
$Pd_{1,5}$	0.245	0.393	0.148	0.141	0.019
$Pt_{1,5}$	0.306	0.375	0.069	0.086	−0.004

By comparing various bond distances as a function of metal characteristics and cluster size, the effect of changing the cluster on the adsorption of a CO or O_2 molecule can be determined. Equation (4) defines the distance parameter Δr_N as the difference between the metal−O (surface) distance for a single metal atom (M_1) or supported pure metal cluster (M_5) and the corresponding distance when the supported atom/cluster has an adsorbed CO or O_2 molecule:

$$\Delta r_N = r_{X_N(\mathrm{Mol})} - r_{X_N}, \quad (4)$$

where $N = 1$ or 5 and Mol = CO or O_2.

Equation (5) quantifies the effect of cluster size on the length variations of M−C, M−O, C−O and O−O bonds for all metals M, by comparing various metal-support, metal-molecule and intramolecular bond distances for the pure supported cluster (M_5) and the single atom (M_1):

$$\Delta r_{1\to5}^{AB} = r_{X_1(\mathrm{Mol})}^{AB} - r_{X_5(\mathrm{Mol})}^{AB}, \quad (5)$$

where AB = MO* labels the average bond distance between the metal atom (or cluster metal atoms) and oxygen atoms of MgO and AB = MC, MO labels the bond distance between the metal atom (cluster metal atoms) and the adsorbed CO or O_2 molecule; and AB = CO, OO labels the C–O or O–O bond length of the adsorbed molecule. Values of these distance parameters are listed in Tables 3 and 4 for CO and O_2 adsorption, respectively. Upon adsorption of CO and O_2 molecules, except for the O−O bond length on the supported Pt_5 cluster, going from a single atom to the pentameric cluster, all bonds (see Tabs. 3 and 4) are slightly longer. The prediction that CO adsorption on single MgO-supported atoms leads to elongation of the metal-oxygen (substrate) bond (see Tab. 3) was previously observed by Broqvist and Grönbeck [72] for Pd, Pt and Ag.

The lowest energy structures of the supported pure and mixed pentameric clusters, following CO or O_2 adsorption are shown in Figure 5. Figure 5a shows that the CO molecule binds preferentially to bridging sites between two metal atoms, with the exceptions of Pd_1Au_4 (CO bound to a Pd atom), Pd_3Pt_2 (CO on Pt) and Pd_5 (CO caps a Pd_3 face). Generally, the CO molecule prefers to adsorb on apical cluster sites because these sites generally carry more negative charge. For the GM structure of supported Pd_1Au_4, the Pd atom is at the cluster–substrate interface (see Fig. 2a) but the adsorption of CO to the cluster leads to a distortion of the cluster structure (see Fig. 5a), so the CO molecule can bind directly to the Pd atom. Therefore, the adsorption of CO provides a driving force

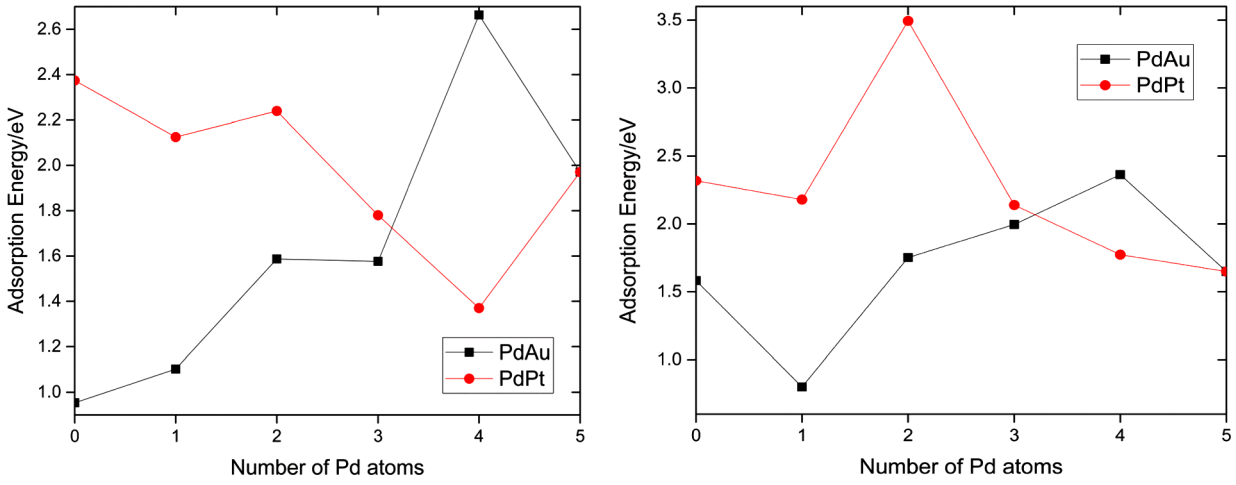

Fig. 4. Adsorption energies of (a) CO and (b) O_2 on supported pentameric PdAu and PdPt clusters.

for rearranging the supported cluster. This was previously observed for O_2 adsorbed on MgO-supported Pd [73] and Au [74] clusters. The general trend in the adsorption energy of CO on cluster metal sites is Pt > Pd > Au, as for the M_1-CO adsorption energies described above. The bonding between CO and metal atoms/clusters is associated with the balance between CO to metal electron (σ) donation and metal to (π) CO back-donation. Due to its higher electron affinity, Au exhibits least electron sharing, and therefore Au–CO bonding is generally weak. An experimental study conducted by Judai et al. [75] showed that comparing Ag, Rh and Pd atoms on MgO thin films, the interaction of CO on supported Ag atoms is the weakest and does not lead to stable structures. Figure 4a shows that CO adsorption energies are generally higher on PdPt (with CO usually bound to a Pt atom or bridging a Pt_2 or PdPt edge of the cluster) than on PdAu clusters. However, Figure 4a also shows that the highest CO adsorption energy (2.66 eV) is actually calculated for Pd_4Au_1.

Adsorption and activation of molecular O_2 by the catalyst are necessary elementary steps in the CO oxidation process. The adsorption of small molecules determines the applicability of a cluster or nanoparticle as a reactive species. Our results indicates that molecular (non-dissociative) adsorption of O_2 on the supported clusters is favorable except for Pd_2Pt_3, where barrierless dissociation and oxygen migration (generating two adsorbed O atoms) is observed (see Fig. 5b), resulting in two oxygen-bridged Pd–Pt edges. This explains why Pd_2Pt_3 has the highest O_2 adsorption energy (3.49 eV, see Fig. 4b), since the total adsorption energy of two oxygen atoms is greater than for non-dissociative adsorption of an O_2 molecule. The adsorption characteristics of O_2 exhibits similar trends to CO adsorption on the supported clusters, though the metal−O_2 adsorption energies are typically higher than for metal−CO. The best candidate for trapping O_2 molecules is Pt, while, Au sites have the weakest ability to trap O_2 molecules, as can be seen from Figures 4b and 5b. In addition to O_2 dissociation, several other adsorption modes are found. Terminal coordination, where O_2 is bound to a single metal atom through one oxygen atom, is observed on Au (in $PdAu_4$), on Pd (e.g. in Pd_3Au_2) and on Pt (e.g. on Pt_5). Pd_2Au_3 has side-on (π-type) bonding of O_2 on a Pd atom which is also bound to the MgO surface. There are two edge-bridging binding modes, either where the O_2 molecule bridges via a single oxygen atom (as in Au_5 and Pd_4Au, bridging Au_2 and Pd_2 edges, respectively) or where both ends of the molecule are bound across the edge (Pd_3Pt_2, bridging a Pd–Pt edge).

4 Conclusion

We have used the S-BCGA approach (at the DFT level of theory) to perform a comparative computational study of the structures, interaction energies and magnetic properties of 5-atom PdAu and PdPt clusters (across the full range of compositions) on a MgO(1 0 0) support. We have then considered the strength of adsorption of CO and O_2 molecules on the supported clusters, identifying preferred binding sites and also noting adsorbate-induced changes in the cluster structures. The cluster structures exhibit clear doping trends, in which Pt preferentially binds to the surface of the oxide support whereas Au preferentially binds in peripheral apical positions away from the interface. Metal–metal bond strengths vary in the order Pt > Pd > Au. Pt and Au promote 2D structural motifs while Pd favors 3D motifs, following Volmer–Weber growth. Due to relatively strong Pt–O binding, Pt atoms preferentially segregate to the cluster–substrate interface and strengthen the interaction with the MgO surface. This will reduce the diffusion of the clusters on the substrate and help to prevent catalyst sintering. Calculation of the excess energies shows that all the bimetallic clusters are stable relative to disproportionation to the monometallic clusters.

The adsorption of O_2 is stronger than that of CO on the supported clusters, which can be attributed to the strong hybridization between the metal-*d* and O-*p* orbitals. We also found that the supported Pd_2Pt_3 cluster spontaneously dissociates the O_2 molecule. Au exhibits the weakest CO-metal interaction while Pt forms

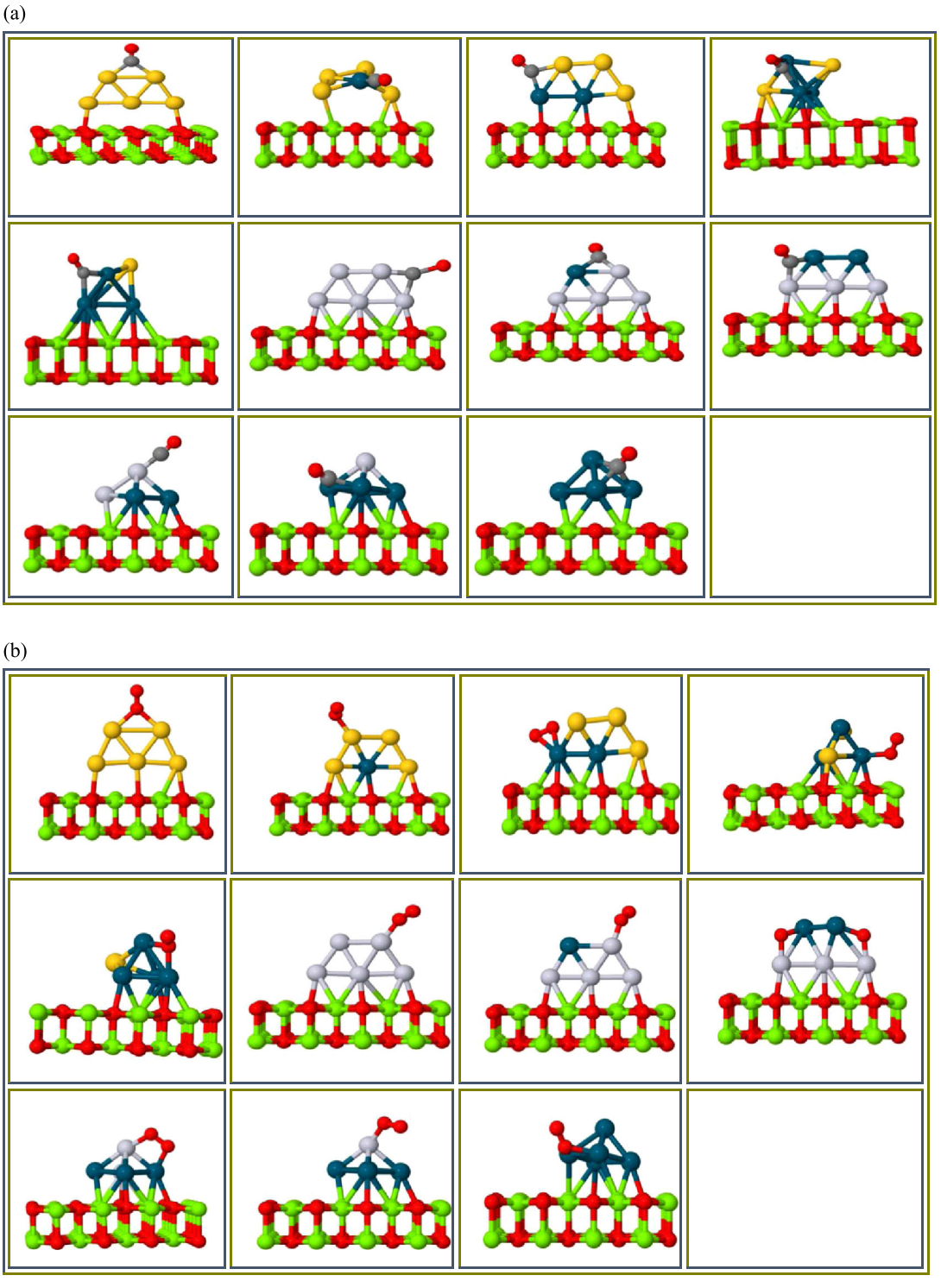

Fig. 5. Structures of the lowest energy configuration for each composition of supported pentameric PdAu and PdPt clusters after (a) CO and (b) O_2 adsorption. Au, Pd, Pt, Mg, O and C are colored gold, cyan, white, green, red and grey, respectively.

the strongest interactions to CO. Adsorption of CO or O_2 leads to a weakening of cluster–surface interaction, which may increase the mobility of the cluster on MgO, perhaps leading to enhanced sintering under catalytic conditions. The adsorption of a CO molecule on the supported Pd_1Au_4 cluster leads to a rearrangement of the cluster structure, allowing direct Pd–CO bonding (which is stronger than Au–CO bonding) to take place. Synergistic effects have been identified, which enable tuning of the characteristics of the clusters and these are likely to be in the design of active and selective, surface-supported subnanometre cluster catalysts.

In the future, the investigation we have performed will be extended to other metal clusters, substrates and adsorbates, where the dependence of chemical ordering and structure on the composition will be analyzed, including effects due to dispersion [76].

Supplementary material

Table S1. Variation of energies for reminimised global minimum structures as a function of the number of unpaired electrons, for each composition of supported PdAu and PdPt clusters.
Table S2. Bond lengths for supported PdAu and PdPt clusters with/without CO and O_2 adsorption.
Table S3. Energies of supported Au_5 structures with respect to the various k meshes.

The authors are grateful to Heider A. Hussein for helpful discussions. The calculations reported here were performed on the following HPC facilities: The University of Birmingham BlueBEAR facility (see http://www.bear.bham.ac.uk/bluebear), the MidPlus Regional Centre of Excellence for Computational Science, Engineering and Mathematics, funded under EPSRC grant EP/K000128/1; and via membership of the UK's HPC Materials Chemistry Consortium, funded by EPSRC (EP/L000202), this work made use of the facilities of ARCHER, the UK's national high-performance computing service, which is funded by the Office of Science and Technology through EPSRC's High End Computing Programme. MA acknowledges financial support by The Scientific and Technological Research Council of Turkey (TUBITAK).

Author contribution statement

MA designed the research project and carried out the calculations. MA and RLJ both analyzed the results and wrote the paper.

References

1. G. Fiori, F. Bonaccorso, G. Iannaccone, T. Palacios, D. Neumaier, A. Seabaugh, S.K. Banerjee, L. Colombo, Nat. Nanotechnol. **9**, 768 (2014)
2. S.B. Sinnott, E.C. Dickey, Mater. Sci. Eng.: R: Rep. **43**, 1 (2003)
3. A. Mugarza, R. Robles, C. Krull, R. Korytár, N. Lorente, P. Gambardella, Phys. Rev. B **85**, 155437 (2012)
4. H. Kwak, S. Chaudhuri, J. Alloys Compd. **509**, 8189 (2011)
5. Y. Li, A.I. Frenkel, in *XAFS techniques for catalysts, nanomaterials, and surfaces* (Springer International Publishing, AG Switzerland, 2017), p. 273
6. D. Uzio, G. Berhault, Catal. Rev. **52**, 106 (2010)
7. S. Vajda, M.J. Pellin, J.P. Greeley, C.L. Marshall, L.A. Curtiss, G.A. Ballentine, J.W. Elam, S. Catillon-Mucherie, P.C. Redfern, F. Mehmood, Nat. Mater. **8**, 213 (2009)
8. W.-N. Wang, W.-J. An, B. Ramalingam, S. Mukherjee, D.M. Niedzwiedzki, S. Gangopadhyay, P. Biswas, J. Am. Chem. Soc. **134**, 11276 (2012)
9. F. Baara, A. Chemam, *Presented at the IOP Conference Series: Materials Science and Engineering, 2016* (unpublished)
10. F.A. Al-Doghachi, U. Rashid, Z. Zainal, M.I. Saiman, Y.H.T. Yap, RSC Adv. **5**, 81739 (2015)
11. L. Sementa, G. Barcaro, A. Fortunelli, Inorg. Chim. Acta **431**, 150 (2015)
12. Z. Yang, R. Wu, Q. Zhang, D. Goodman, Phys. Rev. B **65**, 155407 (2002)
13. M. Sterrer, T. Risse, L. Giordano, M. Heyde, N. Nilius, H.P. Rust, G. Pacchioni, H.J. Freund, Angew. Chem. Int. Ed. **46**, 8703 (2007)
14. A. Shayeghi, D. Götz, J. Davis, R. Schaefer, R.L. Johnston, Phys. Chem. Chem. Phys. **17**, 2104 (2015)
15. C.J. Heard, S. Vajda, R.L. Johnston, J. Phys. Chem. C **118**, 3581 (2014)
16. S. Lee, B. Lee, F. Mehmood, S. Seifert, J.A. Libera, J.W. Elam, J. Greeley, P. Zapol, L.A. Curtiss, M.J. Pellin, J. Phys. Chem. C **114**, 10342 (2010)
17. H. Grönbeck, P. Broqvist, J. Chem. Phys. **119**, 3896 (2003)
18. C.R. Henry, Prog. Surf. Sci. **80**, 92 (2005)
19. B. Pauwels, G. Van Tendeloo, W. Bouwen, L.T. Kuhn, P. Lievens, H. Lei, M. Hou, Phys. Rev. B **62**, 10383 (2000)
20. A. Sanchez, S. Abbet, U. Heiz, W.-D. Schneider, H. Häkkinen, R. Barnett, U. Landman, J. Phys. Chem. A **103**, 9573 (1999)
21. Z. Li, C.V. Ciobanu, J. Hu, J.-P. Palomares-Baez, J.-L. Rodríguez-López, R. Richards, Phys. Chem. Chem. Phys. **13**, 2582 (2011)
22. L. Sementa, G. Barcaro, F.R. Negreiros, A. Fortunelli, Phys. Chem. Chem. Phys. **16**, 26570 (2014)
23. G. Barcaro, A. Fortunelli, Faraday Discuss. **138**, 37 (2008)
24. J.B. Davis, S.L. Horswell, R.L. Johnston, J. Phys. Chem. C **120**, 3759 (2016)
25. A. Roldaìn, J.M. Ricart, F. Illas, G. Pacchioni, J. Phys. Chem. C **114**, 16973 (2010)
26. G. Ertl, M. Neumann, K. Streit, Surf. Sci. **64**, 393 (1977)
27. X.-N. Li, Z. Yuan, S.-G. He, J. Am. Chem. Soc. **136**, 3617 (2014)
28. F.R. Negreiros, L. Sementa, G. Barcaro, S. Vajda, E. Apraì, A. Fortunelli, ACS Catal. **2**, 1860 (2012)
29. F. Wang, D. Zhang, Y. Ding, J. Phys. Chem. C **114**, 14076 (2010)
30. Z. Duan, G. Henkelman, Phys. Chem. Chem. Phys. **18**, 5486 (2016)
31. W.A. Halim, S.A. Aal, A. Shalabi, Thin Solid Films **516**, 4360 (2008)
32. A.V. Matveev, K.M. Neyman, I.V. Yudanov, N. Rösch, Surf. Sci. **426**, 123 (1999)
33. V.A. Nasluzov, V.V. Rivanenkov, A.B. Gordienko, K.M. Neyman, U. Birkenheuer, N. Rösch, J. Chem. Phys. **115**, 8157 (2001)
34. L. Giordano, C. Di Valentin, G. Pacchioni, J. Goniakowski, Chem. Phys. **309**, 41 (2005)

35. R. Ferrando, J. Jellinek, R.L. Johnston, Chem. Rev. **108**, 845 (2008)
36. P. Liu, J.K. Nørskov, Phys. Chem. Chem. Phys. **3**, 3814 (2001)
37. F. Maroun, F. Ozanam, O. Magnussen, R. Behm, Science **293**, 1811 (2001)
38. M. Chen, K. Luo, T. Wei, Z. Yan, D. Kumar, C.-W. Yi, D. Goodman, Catal. Today **117**, 37 (2006)
39. J. Feng, C. Ma, P.J. Miedziak, J.K. Edwards, G.L. Brett, D. Li, Y. Du, D.J. Morgan, G.J. Hutchings, Dalton Trans. **42**, 14498 (2013)
40. R. Ferrando, G. Rossi, A.C. Levi, Z. Kuntová, F. Nita, A. Jelea, C. Mottet, G. Barcaro, A. Fortunelli, J. Goniakowski, J. Chem. Phys. **130**, 174702 (2009)
41. C.J. Heard, S. Heiles, S. Vajda, R.L. Johnston, Nanoscale **6**, 11777 (2014)
42. M. Polak, L. Rubinovich, Surf. Sci. **584**, 41 (2005)
43. D. Wales, J. Doye, J. Phys. Chem. A **101**, 5111 (1997)
44. R.L. Johnston, Dalton Trans. **22**, 4193 (2003)
45. M. Aslan, J.B. Davis, R.L. Johnston, Phys. Chem. Chem. Phys. **18**, 6676 (2016)
46. P. Giannozzi, S. Baroni, N. Bonini, M. Calandra, R. Car, C. Cavazzoni, D. Ceresoli, G.L. Chiarotti, M. Cococcioni, I. Dabo, J. Phys.: Condens. Matter **21**, 395502 (2009)
47. A.M. Rappe, K.M. Rabe, E. Kaxiras, J. Joannopoulos, Phys. Rev. B **41**, 1227 (1990)
48. D. Vanderbilt, Phys. Rev. B **32**, 8412 (1985)
49. J.P. Perdew, K. Burke, M. Ernzerhof, Phys. Rev. Lett. **77**, 3865 (1996)
50. M. Methfessel, A. Paxton, Phys. Rev. B **40**, 3616 (1989)
51. F. Buendía, J.A. Vargas, M.R. Beltrán, J.B. Davis, R.L. Johnston, Phys. Chem. Chem. Phys. **18**, 22122 (2016)
52. L. Xu, G. Henkelman, C.T. Campbell, H. Jónsson, Phys. Rev. Lett. **95**, 146103 (2005)
53. A. Bogicevic, D.R. Jennison, Surf. Sci. **437**, L741 (1999)
54. L. Giordano, G. Pacchioni, Surf. Sci. **575**, 197 (2005)
55. G. Barcaro, A. Fortunelli, New J. Phys. **9**, 22 (2007)
56. G. Barcaro, A. Fortunelli, J. Chem. Theory Comput. **1**, 972 (2005)
57. H. Häkkinen, M. Moseler, U. Landman, Phys. Rev. Lett. **89**, 033401 (2002)
58. R. Ismail, R. Ferrando, R.L. Johnston, J. Phys. Chem. C **117**, 293 (2012)
59. G. Zanti, D. Peeters, J. Phys. Chem. A **114**, 10345 2010
60. H.A. Hussein, J.B. Davis, R.L. Johnston, Phys. Chem. Chem. Phys. **18**, 26133 (2016)
61. E. Bauer, Zeitsch. Kristallogr. **110**, 372 (1958)
62. Y.-L. Hu, W.-B. Zhang, Y.-H. Deng, B.-Y. Tang, Comput. Mater. Sci. **42**, 43 (2008)
63. Y. Wang, H. Gao, J. Phys. Chem. B **121**, 2132 (2017)
64. B.L. Chittari, V. Kumar, Phys. Rev. B **92**, 125442 (2015)
65. A.S. Chaves, G.G. Rondina, M.J. Piotrowski, P. Tereshchuk, J.L.F. Da Silva, J. Phys. Chem. A **118**, 10813 (2014)
66. Y. Watanabe, X. Wu, H. Hirata, N. Isomura, Catal. Sci. Technol. **1**, 1490 (2011)
67. C. Kittel, *Introduction to solid state physics* (Wiley, New York, 2005)
68. J.B. Davis, R.L. Johnston, L. Rubinovich, M. Polak, J. Chem. Phys. **141**, 224307 (2014)
69. I.A. Pašti, M.R. Baljozoviæ, L.P. Granda-Marulanda, N.V. Skorodumova, Phys. Chem. Chem. Phys. **17**, 9666 (2015)
70. K. Neyman, C. Inntam, V. Nasluzov, R. Kosarev, N. Rösch, Appl. Phys. A: Mater. Sci. Process. **78**, 823 (2004)
71. M.B. Knickelbein, Phys. Rev. Lett. **86**, 5255 (2001)
72. H. Grönbeck, P. Broqvist, J. Phys. Chem. B **107**, 12239 (2003)
73. G. Kwon, G.A. Ferguson, C.J. Heard, E.C. Tyo, C. Yin, J. DeBartolo, S.N. Seifert, R.E. Winans, A.J. Kropf, J. Greeley, ACS Nano **7**, 5808 (2013)
74. L.B. Vilhelmsen, B. Hammer, Phys. Rev. Lett. **108**, 126101 (2012)
75. K. Judai, S. Abbet, A.S. Wörz, U. Heiz, L. Giordano, G. Pacchioni, J. Phys. Chem. B **107**, 9377 (2003)
76. J.B.A. Davis, F. Baletto, R.L. Johnston, J. Phys. Chem. A **119**, 9703 (2015)